SCIENCE CHINA
Information Sciences

• RESEARCH PAPER •

April 2020, Vol. 63 140903:1–140903:12
https://doi.org/10.1007/s11432-019-2768-1

Special Focus on Exploring the Far Side of the Moon — the Preliminary Data From Chang'e-4 Mission

Mineralogy of Chang'e-4 landing site: preliminary results of visible and near-infrared imaging spectrometer

Jian CHEN[1], Zongcheng LING[1*], Le QIAO[1], Zhiping HE[2], Rui XU[2], Lingzhi SUN[3], Jiang ZHANG[1], Bo LI[1], Xiaohui FU[1], Changqing LIU[1] & Xiaobin QI[1]

[1]*Shandong Key Laboratory of Optical Astronomy and Solar-Terrestrial Environment, School of Space Science and Physics, Institute of Space Sciences, Shandong University, Weihai* 264209*, China;*
[2]*Key Laboratory of Space Active Opto-Electronics Technology, Shanghai Institute of Technical Physics, Chinese Academy of Sciences, Shanghai* 200083*, China;*
[3]*Hawai'i Institute of Geophysics and Planetology, Department of Earth Sciences, University of Hawai'i at Mānoa, Honolulu* HI 96826*, USA*

Received 11 June 2019/Revised 3 September 2019/Accepted 20 December 2019/Published online 9 March 2020

Abstract The exploration of mafic anomaly in South Pole-Aitken (SPA, the largest confirmed) basin on the Moon provides important insights into lunar interior. The landing of Chang'e-4 (CE-4) and deployment of Yutu-2 rover on the discontinuous ejecta from Finsen crater enabled *in-situ* measurements of the unusual mineralogy in the central portion of SPA basin with visible and near-infrared imaging spectrometer (VNIS). Here we present detailed processing procedures based on the level 2B data of CE-4 VNIS and preliminary mineralogical results at the exploration area of Yutu-2 rover. A systematic processing pipeline is developed to derive credible reflectance spectra, based on which several spectral and mineral indices are calculated to constrain the mafic mineralogy. The mafic components in the soils and boulder around CE-4 landing site are concluded as clinopyroxene-bearing with intermediate composition and probably dominated by pigeonite although the possibility of mixing orthopyroxen (OPX) and calcic clinopyroxene (CPX) also exists. These mineralogical results are more consistent with a petrogenesis that the CE-4 regolith and rock fragment are derived from rapid-cooling magmatic systems and we interpret that the materials at the CE-4 landing site ejected from Finsen crater are probably recrystallized from impact melt settings.

Keywords Chang'e-4, visible and near-infrared spectroscopy, mineralogy, impact melt, the Moon

Citation Chen J, Ling Z C, Qiao L, et al. Mineralogy of Chang'e-4 landing site: preliminary results of visible and near-infrared imaging spectrometer. Sci China Inf Sci, 2020, 63(4): 140903, https://doi.org/10.1007/s11432-019-2768-1

1 Introduction

The first-ever landing on the farside of the Moon (Figure 1) was realized by Chang'e-4 (CE-4) mission with its successful touchdown in the South Pole-Aitken (SPA) basin on 3 January 2019 [1–3]. As the largest confirmed impact basin on the Moon [4], SPA basin is thought to have penetrated into lunar interior and excavated deep materials from lower crust and upper mantle during its formation [5–7]. Since global remote sensing enabled observations of the lunar farside, numerous researches have been performed on SPA basin with various orbital datasets. Observations of the SPA basin floor indicate that it is characterized by mafic anomaly [5–11] and elevated concentrations of incompatible elements (e.g., Th, [12–14]) and is dominated by low-Ca pyroxene (LCP, orthopyroxene (OPX) or pigeonite)-rich

* Corresponding author (email: zcling@sdu.edu.cn)

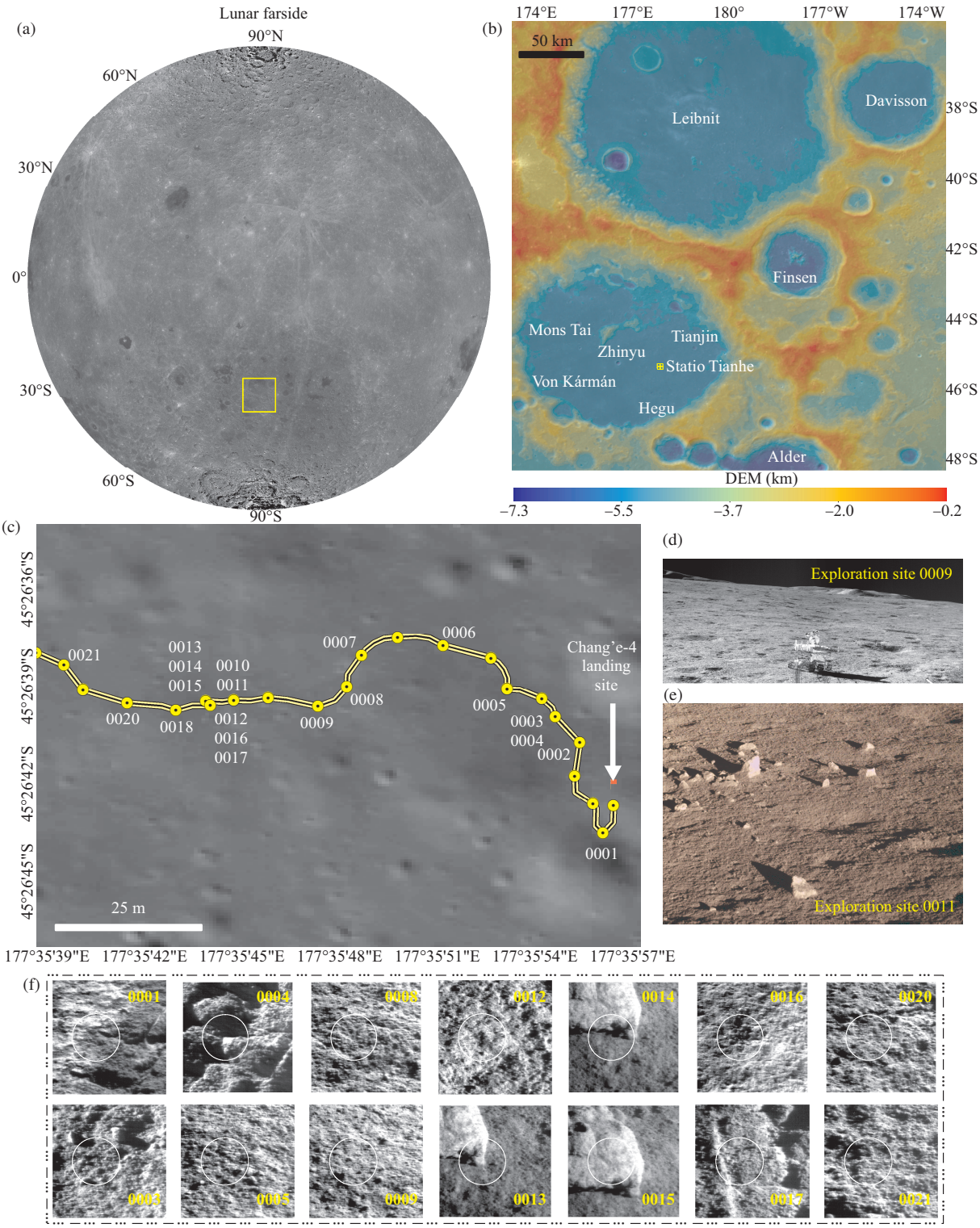

Figure 1 (Color online) Global to ground view of the CE-4 landing site, exploration region of Yutu-2 rover, and the VNIS detections. (a) CE-1 digital orthophoto map (DOM) of lunar farside. The yellow indicator shows the extent of frame (b). (b) Nomenclature surrounding CE-4 landing site on CE-2 digital elevation model (DEM) and DOM. (c) Traverse path of Yutu-2 rover and location of exploration sites during the first three lunar days on image taken by the CE-4 landing camera (LCAM), each exploration site is marked by yellow circles and its number which corresponds that in panel (f). (d) Image of Yutu-2 rover at exploration site 0009 acquired by the CE-4 terrane camera (TCAM). (e) Boulders viewed by the CE-4 panoramic camera (PCAM) at the exploration site 0011. (f) 900-nm-band images of 14 VNIS detections. The white circles show the field of view of short-wave infrared (SWIR) detectors.

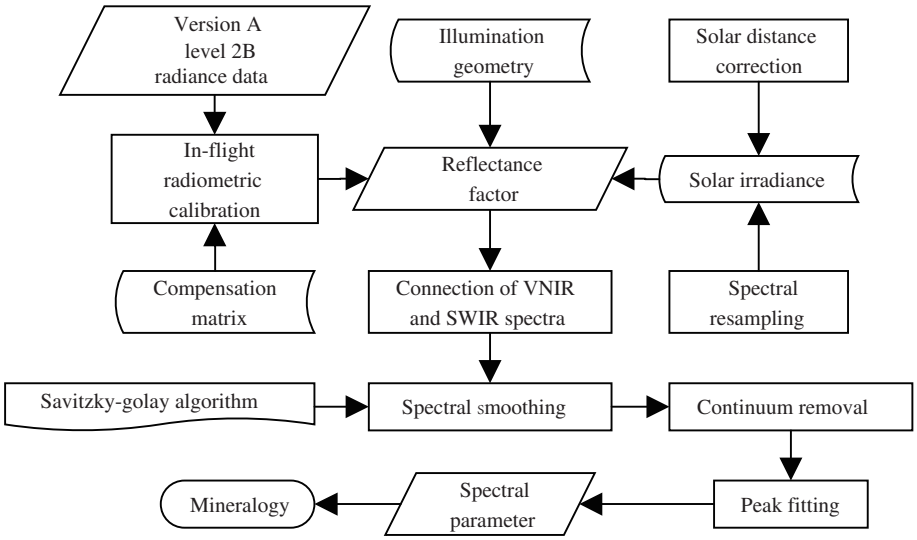

Figure 2 Processing procedures based on CE-4 VNIS level 2B radiance data.

noritic materials with disperse high-Ca pyroxene (HCP)-rich gabbroic or basaltic lithologies (e.g., [5,7–9]) compared to the feldsparthic highlands outside of the basin. Among diverse aspects of SPA region, the nature of mafic anomaly in the floor of SPA basin, which exhibits distinct geochemical and spectral characteristics from returned lunar samples and currently known lunar meteorites [5–14], is regarded as an ideal indicator of the composition and mineralogy of lunar interior (lower crust or upper mantle).

The CE-4 landing site is located on the floor of ancient Pre-Nectarian Von Kármán crater, where it is flooded by low-TiO_2 mare basaltic lava flows and then mostly overprinted by discontinuous ejecta from the nearby Finsen crater in the northeast [15–22]. The ejecta, characterized by non-mare mafic components in orbital remote sensing datasets, exhibits pervasive mineralogical similarities to the mafic anomaly observed in the central portion of SPA basin [8]. Different from all previous studies based on orbital datasets in the past, the *in-situ* spectroscopic observation datasets of Finsen ejecta around the CE-4 landing site acquired by the visible and near-infrared imaging spectrometer (VNIS) onboard the Yutu-2 rover provide a valuable opportunity to improve our understanding of the unusual mineralogy in the floor of SPA basin. This study aims to develop a systematic VNIS data processing strategy and report preliminary analysis results in terms of mineralogical information of the exploration region of Yutu-2 rover in the first three lunar days.

2 Data and methods

2.1 VNIS data

The VNIS collected hyperspectral visible and near-infrared (VNIR) images (450–950 nm) and single-pixel short-wave infrared (SWIR) spectra (900–2400 nm) for fourteen detection targets during the first three lunar days of CE-4 mission. The locations of the VNIS measurements are shown in Figure 1. The VNIS raw data are reduced into level 2B radiance through a series of processing pipelines including dark-current, scattering-background subtractions, flat-field, instrument temperature corrections, and radiometric and geometric calibrations [23, 24], and then distributed by the Ground Research and Application System (GRAS) of Chinese Lunar Exploration Program. The level 2B VNIS radiance data are further processed to extract diagnostic absorption characteristics and identify the surface mineralogy of exploration sites in this study. The processing procedures based on level 2B VNIS radiance data are shown in Figure 2.

2.2 Reflectance calculation

Because the VNIS version A level 2B radiance data distributed by GRAS are generated with the radiometric calibration matrix obtained from ground/pre-flight experiments, a compensation matrix from in-flight radiometric calibration experiments is applied to VNIS level 2B radiance data to correct various effects owing to the change of working environment of the instrument. Afterwards, the corrected radiance data are converted to reflectance factor by (1) to eliminate the Fraunhofer lines inherited from the incident sunlight and emphasize the absorption features related to minerals on the lunar surface.

$$\mathrm{REFF}\,(i,e,g,\lambda)=\frac{\pi L\,(\lambda)}{\cos\,(i)\,\frac{1}{D^2}\int F\,(\lambda)\,T\,(\lambda)\,\mathrm{d}\lambda}, \tag{1}$$

where REFF is the reflectance factor. i, e, and g are the incidence, emission, and phase angles. $L(\lambda)$ is radiometrically corrected radiance data. D is the Sun-Moon distance in a unit of astronomical unit (AU) and is calculated for the VNIS data according to the observation time of each band, with the NASA NAIF SPICE Toolkit and SPICE kernels naif0012.tls, pck00010.tpc, and DE438.bsp[1)]. $\frac{1}{D^2}\int F\,(\lambda)\,T\,(\lambda)\,\mathrm{d}\lambda$ is spectral resampling and distance correction for solar irradiance, where $F(\lambda)$ is the extraterrestrial solar irradiance data without terrestrial atmospheric absorptions [25] and $T(\lambda)$ is the spectral response function of detectors. The solar irradiance data are reported at a spectral resolution distinct from that of VNIS and a standard distance of 1 AU [25], hence, the solar irradiance data must be resampled with the spectral response function of VNIS and corrected to the Sun-Moon distance during VNIS detections by a factor of D^2.

As the CE-4 VNIS measurements are performed at large phase angles ($\sim 65°$–$105°$ for SWIR data during the first three lunar days), photometric correction is important for comparisons of reflectance spectra taken under different illumination conditions and further quantitative analysis of mineral abundances for local regolith, while it is not included in this study because photometric correction has negligible effects on the continuum removed spectra used in this study, which is reporting preliminary and qualitive analysis results of mineralogy. A robust photometric model for CE-4 landing site could be derived from VNIS data collected in the fourth and tenth lunar day when spectral measurements at various illumination geometry are done by Yutu-2 rover (i.e., covering a large range of phase angles).

2.3 Connection of VNIR and SWIR spectra

The field of view (FOV) of the single-pixel SWIR detector is corresponding to a circular region with a diameter of 107.6 pixels (a radius of 53.8 pixels) and centered at the coordinate (98, 127.5) within the FOV of the VNIR image [26]. The distance of each pixel in VNIR image to the circle center is calculated as follows:

$$\mathrm{Distance}=\sqrt{(x-98)^2+(y-127.5)^2}, \tag{2}$$

where x and y are the center coordinates of each pixel. If the distance is less than the radius (53.8), the pixel is considered as in the FOV of SWIR detector. In this study, 9104 pixels in the VNIR hyperspectral image are concluded to be covered by the FOV of SWIR detector. For each of the fourteen detections, VNIR spectral data of these 9104 pixels are averaged and smoothed using the Savitzky-Golay (SG) algorithm [27], which essentially performs a polynomial regression and convolution to the spectral data points in a moving window. The smoothed VNIR spectrum is then connected with the SWIR spectrum measured from the circle FOV. To fix the step artifacts resulted from the response differences of the detectors, factors obtained at 900 nm and 1375–1380 nm of the SWIR spectrum are used to correct the VNIR spectra in 450–900 nm region and the SWIR spectra in 900–1375 nm region, respectively. The description and correction of artifacts at 1375–1380 nm and 900–945 nm are presented in Appendix A. The combined spectra are then treated with SG smoothing procedure, because CE-4 VNIS reflectance spectra present noisy (fluctuant) variations with wavelength (e.g., Figure S1). SG smoothing is used

1) http://naif.jpl.nasa.gov.

to suppress the effects of local noises on the automatic detection of tie points for continuum removal with tangency line method and on the calculation of spectral parameters afterwards. The uncertainties introduced by SG smoothing are discussed in Appendix B.

2.4 Continuum removal

The absorption bands of mafic minerals in lunar reflectance spectra are usually superimposed on a continuum, which is induced by a combination of complex effects from various mineralogical and non-mineralogical factors (e.g., SMFe, submicron Fe produced from space weathering [28, 29]). Therefore, an important step in mineralogical analysis based on reflectance spectra is to estimate and remove the continuum from the raw reflectance spectra, leaving only the absorption bands, of which positions and widths are more dependent on mineralogy (e.g., [30–32]). Because the exact form of continuum as a function of wavelength or energy (wavenumber) is unknown, it is difficult to model the continuum [33]. This study employs tangent line method (Appendix C) to remove the continuum of CE-4 reflectance spectra. The tangent line method is chosen because it automatically detects tie points of continuum whose wavelength ranges vary with mineralogy (e.g., ∼725 nm and ∼1430 nm for LCP, ∼750 nm and ∼1500 nm for HCP, and ∼675 nm and ∼1700 nm for olivine in Appendix D). Therefore, tangency line method is more sensitive to the potential mineralogical differences among different sites explored by Yutu-2 rover compared to those methods which set tie points at fixed wavelengths. Convex hull method is popular for continuum removal of other lunar VNIR hyperspectral remote sensing datasets (e.g., Moon Mineralogy Mapper (M^3) [34–36]) while it is not suitable for continuum removal of 2000 nm absorption in VNIS data, which is not completely measured (Appendixes C and D).

2.5 Spectral fitting

To identify mafic mineralogy at the CE-4 landing site, several spectral indices (e.g., band centers, integrated band depth (IBD) of 1000 and 2000 nm absorptions, IBD ratio (IBDR), and mineral indices of LCP, HCP, olivine (OL)) sensitive to mineralogy, composition, and mineral mixtures in lunar surface spectra were applied on VNIS data [37, 38]. Following the removal of continuum, the band centers of 1000 nm and 2000 nm (BC1 and BC2) are determined by Gaussian fitting, and other spectral indices are calculated according to the definitions given in Table 1 [39]. The primary indices used to detect mafic minerals in VNIS spectra are LCP_INDEX, HCP_INDEX, and OL_INDEX, which are based on searching for lower reflectance in selected wavelengths inside the absorption bands of their target minerals compared to references outside of the absorption bands (Table 1). The LCP_INDEX is defined to detect the 1000 nm and 2000 nm absorptions of LCP (e.g., OPX or pigeonite) via reduced reflectance at 1080 nm and 1820 nm relative to the reflectance at the spectral shoulder near 1330 nm, and the HCP_INDEX is similarly defined to detect HCP (e.g., augite) via reduced reflectance at 1080 and 2070 nm relative to the reflectance at 1470 m [40, 41]. The OL_INDEX is defined to detect olivine via reduced reflectance at 1050, 1210, 1330, and 1470 nm relative to the continuum value at those wavelengths [41]. Although these mineral indices are designed for compact reconnaissance imaging spectrometer for Mars (CRISM) data, they also could be used on remote sensing spectroscopic data on the Moon because these mafic minerals (LCP, HCP, and OL) share the same VNIR absorption properties on different bodies. While the wavelengths of these mineral indices could be optimized for lunar data, unoptimized indices already prove the capability to distinguish terrestrial LCP, HCP, and OL. As seen in Figure 3 [8, 34, 42–44], OPX exhibits high LCP_INDEX and low HCP_INDEX, and cpxclinopyroxene (CPX) presents high HCP_INDEX and low LCP_INDEX while olivine shows high OL_INDEX, low HCP_INDEX, and low LCP_INDEX.

3 Results and discussion

The VNIS spectra of soils at CE-4 landing site are composed of reddish continuum and weak 1000 nm and 2000 nm absorption bands (Figure 3(a)), suggesting that the soils are heavily space weathered products

Table 1 Definitions of spectral indices used in [39][a)]

Spectral index	Definition
IBD1000	$\sum_{n=0}^{s2-s1} 1 - \frac{R(s1+n)}{R_c(s1+n)}$
IBD2000	$2 \times \sum_{n=0}^{bc2-s3} 1 - \frac{R(s3+n)}{R_c(s3+n)}$
IBDR	$\frac{\text{IBD2000}}{\text{IBD1000}}$
LCP_INDEX	$100 \times \left[\frac{R(1330)-R(1080)}{R(1330)+R(1080)}\right] \times \left[\frac{R(1330)-R(1815)}{R(1330)+R(1815)}\right]$
HCP_INDEX	$100 \times \left[\frac{R(1470)-R(1080)}{R(1470)+R(1080)}\right] \times \left[\frac{R(1470)-R(2067)}{R(1470)+R(2067)}\right]$
OL_INDEX	$1 - \left[0.1 \times \frac{R(1054)}{R_C(1054)} + 0.1 \times \frac{R(1211)}{R_C(1211)}\right] + 0.4 \times \frac{R(1329)}{R_C(1329)} + 0.4 \times \frac{R(1474)}{R_C(1474)}$

a) $s1$, $s2$, and $s3$ are the three points used to define continuum (Figure S3), $bc2$ is the band center of 2000 nm, R is the spectral reflectance data at the given wavelength, and R_C is the continuum value at the given wavelength.

from primary mafic-bearing lithologies [28,29]. Among the fourteen detection targets, the boulder (0013–0015 in Figure 1(f), 3(a) and 3(b)) exhibits the highest reflectance and the strongest 1000 nm and 2000 nm absorption band strength, which is consistent with its immature nature. Regardless of the different space weathering degrees between soils and the boulder, their 1000 nm absorption band centers are fallen in a relatively narrow range between 962.1–981.3 nm (Figure 3(c)), indicating that they are likely cogenetic and mineralogically similar and that the local soils are developed from ever existed boulders by space weathering.

The diagnostic 1000 nm and 2000 nm absorption features within the VNIS spectra can be interpreted as the presence of pyroxene within soils and boulder around the CE-4 landing site. The olivine-rich mineralogy as reported in previous studies on CE-4 VNIS spectra [16,18] is likely to be an illusion caused by inappropriate continuum removal method. The convex hull method was used by Li et al. [18] and Gou et al. [16] to estimate the continuum of VNIS spectra where the last band (2395 nm) is on the hull, while the last band should not be on the continuum because the 2000 nm absorption is not completely measured by VNIS (see more basic knowledges of lunar VNIR reflectance spectra in Appendix D). Such a continuum connecting the short-wavelength edge of 2000 nm absorption and the endpoint of VNIS spectra significantly attenuates the true absorption strength at 2000 nm (Figure S3) and generates the illusion that the 2000 nm absorption of VNIS spectra is weak and the mineralogy of CE-4 landing site is olivine-rich. In a word, convex hull method is not suitable for continuum removal of 2000 nm absorption of VNIS spectra.

Although the convex hull method works well to remove continuum of 1000 nm absorption, the resulting long-wavelength edges of 1000 nm absorption in CE-4 VNIS spectra are located at ∼1400–1500 nm (Figure 2(b) in [16,18]), which is very different from that of true olivine (typically at ∼1700 nm, Figure S4). This difference between CE-4 VNIS spectra and true olivine-rich spectra observed by CE-3 VNIS is also obvious in Figure 2(b) of [18] while those authors ignored that and still claimed olivine-rich lithologies for CE-4 landing site. In this study, the long-wavelength edges of 1000 nm absorption in continuum removed CE-4 VNIS spectra detected by tangency line method are located at ∼1430–1500 nm, which is comparable to those derived from other continuum removal methods (e.g., convex hull or tie points at fixed wavelengths) and is consistent with the spectral characteristics of pyroxene (Appendix D). Hence, we interpret that the CE-4 VNIS spectral properties are dominated by pyroxene and that olivine is little at CE-4 landing site.

The 1000 nm and 2000 nm absorption band centers of the continuum removed spectra are utilized to further identify the composition of pyroxene. Compared with the absorption band centers of a suite of pyroxenes with composition varying from Mg-rich pyroxene (OPX or pigeonite) to Ca- and Fe-rich CPX (Figure 3(c)), the absorption bands of CE-4 VNIS spectra are located at intermediate wavelengths between those of OPX and calcic CPX from experiments [42], and also between those of Mg-rich pyroxene and calcic CPX-bearing mare basalt remotely observed by M^3, but resemble those of non-mare CPX in the central SPA mafic anomaly [8] and the spectra of pigeonites with relative enrichments of Fe^{2+} ions in M2 sites [45]. Although the 2000 nm absorption band centers of CE-4 VNIS spectra exhibit large

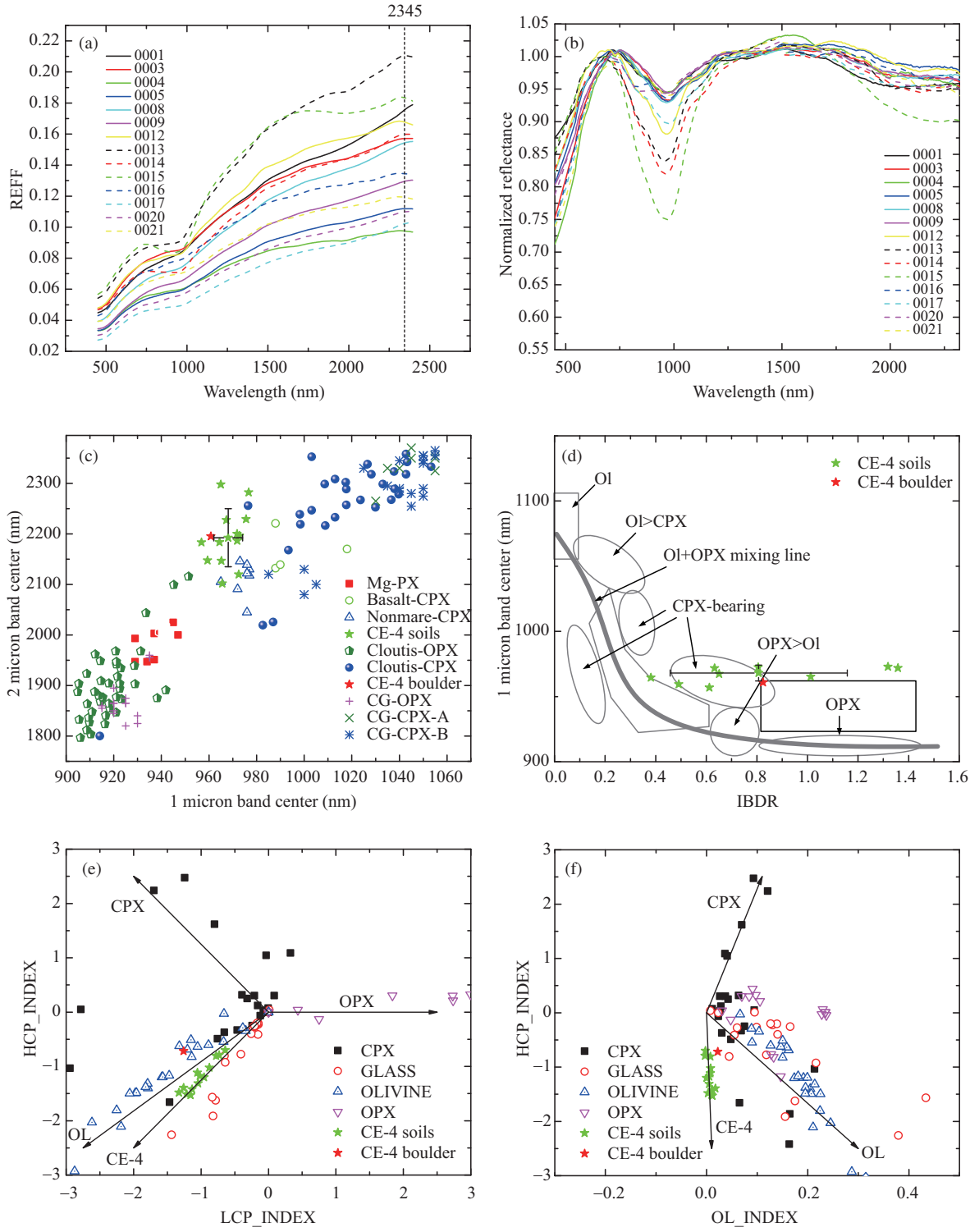

Figure 3 (Color online) VNIS spectra and mineral compositions of Yutu-2 detection sites. (a) Combined VNIS spectra (450–2395 nm) from 14 sites. (b) VNIS spectra after continuum removal. (c) Band center positions of the CE-4 VNIS detection targets overlain on band centers of pyroxene from [8, 42]. (d) BC1-IBDR plot for the fourteen CE-4 VNIS detections. The polygon and elliptic fields represent mineral combinations [34, 43, 44]. The data points with error bars in (c) and (d) represent the average and standard deviations of VNIS spectral parameters. (e) HCP_INDEX vs. LCP_INDEX plot for laboratory spectra [39] of clinopyroxene (black squares), orthopyroxene (purple triangles), olivine (blue triangles), and glass (red circles) and VNIS spectra. (f) HCP_INDEX vs. OL_INDEX plot for the same datasets in (e). Mg-PX: Mg-rich pyroxene; Ol: olivine.

variation from 2110–2264 nm, and slightly deviate from the pyroxene cluster, it is plausible because the long-wavelength edge (typically beyond 2500 nm, Appendix D) of 2000 nm absorption band of pyroxene is not covered by VNIS spectral range (450–2395 nm) so that the continuum removal and spectral fitting of 2000 nm absorption band are subject to large uncertainties (Appendixes B, C, and E).

The band centers of the 1000 nm absorption are plotted against the ratio of IBD2000 to IBD1000 (IBDR, Figure 3(d)) to determine the mafic mineral assemblages that possibly exist at the CE-4 landing site. Data point of the boulder is fallen into the field defined by CPX-bearing lithologies, however the spectra of soils present apparently larger variation of IBD2000 to IBD1000 ratio relative to that of boulder (Figure 3(d)), implying larger uncertainties (Appendixes B and C) of the mitigated absorption bands by strong space weathering or shadow-hiding effects in soil spectra.

Pyroxene and olivine spectral indices (Table 1) are used to evaluate the effects of subtle mineralogical variations in VNIS data. The pyroxene indices of VNIS data reveal that the CE-4 soils and boulder are mineralogically distinct from common OPX and CPX (naturally occurred pyroxenes except pigeonite), and the VNIS data cluster is in a fashion close to the trend line of olivine (Figure 3(e)). However, the OL_INDEX values of VNIS spectra are much lower than those of olivine spectra (Figure 3(f)). A special case of CPX points occurs within the field of VNIS data (Figure 3(e)), in support of the fact that these spectral parameters are generally compromised by minerals with atypical compositions. Hence, based on the spectral inspections above, the dominant spectral properties of the soils at the CE-4 landing site are more consistent with atypical pyroxene composition (e.g., pigeonite).

Besides of the prominent peak at 962–981 nm, an absorption at around 1200 nm contributing to the asymmetric 1000 nm band is observed in CE-4 VNIS spectra. This absorption is also observed in relatively pure anorthosite where small amounts of Fe^{2+} are incorporated into the structure of crystalline plagioclase (e.g., [46–49]). However, this absorption is sensitive to impact events and would disappear under high shock pressures [50, 51]. Hence, the 1200 nm absorption in CE-4 VNIS spectra is not likely contributed by the presence of plagioclase given that the CE-4 landing site is dominated by Finsen's ejecta, which is product of impact events, although we cannot exclude the possibility that recrystallized plagioclase exists in the local soils. Furthermore, the ∼1200 nm feature from plagioclase would be effectively masked by stronger absorptions from mafic minerals when they are present even in small amounts (>15%) (e.g., [52]). On the other hand, the 1200 nm absorption band could be resulted from spin-allowed crystal-field transition of Fe^{2+} in the six-coordinated M1 octahedral crystallographic site of Fe-bearing LCP [49,53,54]. It seems incredible that LCP-dominated lithologies present ferroan compositions considering that LCP-rich non-mare lunar samples returned by Apollo and Luna missions as well as meteorites are virtually magnesian and belong to so called "Mg-suite" [55–57], while it is consistent with the orbital remote sensing results of the SPA basin floor, where the mineralogical maps reveal a LCP-rich character [58, 59] and the geochemical datasets exhibit a ferroan composition [5, 6, 8, 10, 11]. The most prominent 1200 nm absorption band is also often observed in rapidly cooled rocks, because the crystallization occurs quickly enough to preserve a significant proportion of Fe^{2+} occupying the M1 sites of pyroxene, although Fe^{2+} normally prefers the larger M2 site of pyroxene under equilibrium (i.e., slow-cooling) conditions [49, 53, 54].

In summary, the mafic components in the soils and boulder explored by Yutu-2 rover are characterized by CPX with intermediate compositions between HCP and OPX, and probably dominated by low-Ca CPX (i.e., pigeonite), according to the spectroscopic properties of VNIS data and mineralogical identification results in this study. The intermediate pyroxene composition also could be caused by the mixing effect of OPX and calcic CPX. Pigeonite is generally unstable under typical lunar surface environmental condition (low pressures) and thus, is expected to convert into OPX crystal with high-Ca CPX exsolution lamellae as identified in some lunar samples (e.g., [60–63]). Although we do not know whether the pigeonite-like spectra are corresponding to pigeonite or OPX with CPX lamellae (i.e., inverted pigeonite), the occurrence of intermediate pyroxene composition with Fe^{2+} in M1 site at the CE-4 landing site is more consistent with the fast-cooling crystallization condition (e.g., basaltic lava flow or impact melt) at which the pyroxene composition goes into the immiscibility gap between pigeonite and augite [64] and forms solid solution with intermediate composition.

The floor of Von Kármán crater, where the CE-4 landed, was flooded by Imbrian low-TiO_2 mare basalt (LT, [9,15,17,19,21,22]), but the spectral features of CPX at the CE-4 landing site are significantly different from those in typical mare basalts (Figure 3(c)). The Finsen crater is categorized as an Eratosthenian crater (e.g., [8]), whose ray system is thought to be already obscured by space weathering. While the CE-4 landing site is located on the bright ray from Finsen crater, the observed prominent reflectance pattern of the Finsen rays is probably mainly related to compositional contrast with the background mare on the floor of Von Kármán crater, rather than difference of optical maturity [65]. The mineralogy at the CE-4 landing site also shows a strong similarity to those pervasively exposed outcrops on the wall of the Finsen crater (e.g., [5, 8, 21]). Recent spectral and geological investigations using M^3 observation data produced mineralogical maps at an exceptional level of detail and revealed obviously different units (LT and Finsen's ejecta (FE)) on the floor of Von Kármán crater and suggested that the CE-4 landing site has been affected by additional mafic non-mare materials ejected from the wall of Finsen crater (e.g., [15–18]). The dominant mineralogy of FE has been described as LCP-rich (e.g., [20–22]), which is consistent with what the VNIS observes during the *in-situ* explorations.

Considering that SPA region experienced numerous impact events in the long geological history since its formation (e.g., [66]), materials derived from geologic settings of impact melt maybe account for a large proportion of the SPA basin floor. Several previous studies have proposed that the SPA basin forming impact event has extensively melted the mafic cumulates and generated a local magma sea in the floor of the SPA [5, 8, 67–69], in which Mg-rich ultramafic cumulate sank to the base of SPA basin and the modestly evolved residual melt is subsequently deposited as relatively ferroan lithologies at the central portion of SPA. In addition to the ancient SPA basin-forming event, the parental magma of CE-4 soils and boulder also could be sourced from other impact events occurred in SPA region such as Leibnitz crater (Figure 1(b)). Previous studies [16, 18] suggested an origin of lunar mantle materials for CE-4 regolith and rock fragment, while the conclusion is mostly based on the illusion of olivine-rich lithologies as discussed above. According to the perspectives of mineralogy and petrology, the regolith and rock fragment observed by Yutu-2 rover are more likely to be products of rapid-cooling magmatic episodes, rather than fragments of plutonic cumulates from either mantle or the base of a differentiated SPA impact melt sheet. The melting, potential mixing with crustal materials, and recrystallization have blurred the genes inherited from mantle reservoir even if these materials are initially sourced from lunar mantle.

4 Conclusion and future work

We developed a systematic processing pipeline of CE-4 VNIS spectra based on the version A level 2B data to derive credible reflectance spectra. Based on several spectral and mineral indices calculated from the VNIS reflectance spectra, the mafic components in the soils and boulder at CE-4 landing site are concluded as clinopyroxene-bearing and probably dominated by pigeonite, although mixing effect of OPX and calcic CPX cannot be excluded. Such a mafic mineralogy with intermediate pyroxene composition (pigeonite) is more consistent with a petrogenesis that the CE-4 regolith is derived from rapid-cooling magmatic systems (basaltic lava flow or impact melt). The LCP-rich mafic mineralogy and residence on the Finsen's discontinuous ejecta suggest that the soils and boulder observed by Yutu-2 rover are not likely from basaltic lava flows that infill Von Kármán crater, and are probably recrystallized from impact melt settings and delivered to CE-4 landing site by Finsen impact event.

Future work will focus on building a spectral library to derive quantitative modal abundances and mineral compositions (e.g., Mg# (Molar Mg/(Mg+Fe)) of mafic minerals) as well as space weathering degree (abundance of SMFe) with spectral matching. By the extraction of complete mineralogical information from VNIS data, the (crustal or mantle in question) origin of the materials encountered by Yutu-2 rover will be better constrained.

Acknowledgements This work was supported by National Natural Science Foundation of China (Grant Nos. 11941001, 41972322, U1931211), Natural Science Foundation of Shandong Province (Grant No. ZR2019MD008), Qilu Young Scholar (TANG SCHOLAR) Program of Shandong University, Weihai (Grant No. 2015WHWLJH14), Key Research Program of

Frontier Sciences, Chinese Academy of Sciences (Grant No. QYZDY-SSW-DQC028), and Pre-research Project on Civil Aerospace Technologies Funded by China National Space Administration (CNSA) (Grant No. D020102).

Supporting information Appendixes A–E. The supporting information is available online at info.scichina.com and link.springer.com. The supporting materials are published as submitted, without typesetting or editing. The responsibility for scientific accuracy and content remains entirely with the authors.

References

1 Di K, Liu Z, Liu B, et al. Chang'e-4 lander localization based on multi-source data. J Remote Sens, 2019, 23: 177–184
2 Wu W, Li C, Zuo W, et al. Lunar farside to be explored by Chang'e-4. Nat Geosci, 2019, 12: 222–223
3 Liu J, Ren X, Yan W, et al. Descent trajectory reconstruction and landing site positioning of Chang'e-4 on the lunar farside. Nat Commun, 2019, 10: 4229
4 Garrick-Bethell I, Zuber M T. Elliptical structure of the lunar South Pole-Aitken basin. Icarus, 2009, 204: 399–408
5 Hurwitz D M, Kring D A. Differentiation of the South Pole-Aitken basin impact melt sheet: implications for lunar exploration. J Geophys Res Planets, 2014, 119: 1110–1133
6 Lucey P G, Taylor G J, Hawke B R, et al. FeO and TiO_2 concentrations in the South Pole-Aitken basin: implications for mantle composition and basin formation. J Geophys Res, 1998, 103: 3701–3708
7 Pieters C M, Tompkins S, Head J W, et al. Mineralogy of the mafic anomaly in the South Pole-Aitken basin: implications for excavation of the lunar mantle. Geophys Res Lett, 1997, 24: 1903–1906
8 Moriarty Iii D P, Pieters C M. The character of South Pole-Aitken basin: patterns of surface and subsurface composition. J Geophys Res Planets, 2018, 123: 729–747
9 Pieters C M, Head Iii J W, Gaddis L, et al. Rock types of South Pole-Aitken basin and extent of basaltic volcanism. J Geophys Res, 2001, 106: 28001–28022
10 Lawrence D J, Feldman W C, Elphic R C, et al. Iron abundances on the lunar surface as measured by the lunar prospector Gamma-ray and neutron spectrometers. J Geophys Res Planets, 2002, 107: 5130
11 Prettyman T H, Hagerty J J, Elphic R C, et al. Elemental composition of the lunar surface: analysis of gamma ray spectroscopy data from Lunar Prospector. J Geophys Res, 2006, 111: E12007
12 Lawrence D J, Feldman W C, Barraclough B L, et al. Thorium abundances on the lunar surface. J Geophys Res, 2000, 105: 20307–20331
13 Kobayashi S, Karouji Y, Morota T, et al. Lunar farside Th distribution measured by Kaguya gamma-ray spectrometer. Earth Planet Sci Lett, 2012, 337–338: 10–16
14 Jolliff B L, Wieczorek M A, Shearer C K, et al. New Views of the Moon. Gottingan: Mineralogical Society of America, 2018. 60
15 Fu X H, Qiao L, Zhang J, et al. The subsurface structure and stratigraphy of the Chang'e-4 landing site: orbital evidence from small craters on the Von Kármán crater floor. Res Astron Astrophys, 2020, 20: 008
16 Gou S, Di K, Yue Z, et al. Lunar deep materials observed by Chang'e-4 rover. Earth Planet Sci Lett, 2019, 528: 115829
17 Huang J, Xiao Z, Flahaut J, et al. Geological characteristics of Von Kármán crater, northwestern South Pole-Aitken basin: Chang'e-4 landing site region. J Geophys Res Planets, 2018, 123: 1684–1700
18 Li C, Liu D, Liu B, et al. Chang'e-4 initial spectroscopic identification of lunar far-side mantle-derived materials. Nature, 2019, 569: 378–382
19 Ling Z, Jolliff B L, Liu C, et al. Composition, mineralogy, and chronology of mare basalts in Von Kármán crater: a candidate landing site of Chang'e-4. In: Proceedings of the 49th Lunar and Planetary Science Conference, Houston, 2018. 1939
20 Ling Z, Jolliff B L, Liu C, et al. A close view of Chang'e-4 landing site and science questions to be answered by Yutu-2. In: Proceedings of the 50th Lunar and Planetary Science Conference, Houston, 2019. 2330
21 Ling Z, Qiao L, Liu C, et al. Composition, mineralogy and chronology of mare basalts and non-mare materials in Von Kármán crater: landing site of the Chang'e-4 mission. Planet Space Sci, 2019, 179: 104741
22 Qiao L, Ling Z, Fu X, et al. Geological characterization of the Chang'e-4 landing area on the lunar farside. Icarus, 2019, 333: 37–51
23 He Z, Xu R, Li C, et al. Visible and near-infrared imaging spectrometer (VNIS) for *in-situ* lunar surface measurements. In: Proceedings of Sensors, Systems, and Next-Generation Satellites XIX, 2015. 9639
24 Liu B, Li C L, Zhang G L, et al. Data processing and preliminary results of the Chang'e-3 VIS/NIR imaging spectrometer *in-situ* analysis. Res Astron Astrophys, 2014, 14: 1578–1594
25 Gueymard C A. The Sun's total and spectral irradiance for solar energy applications and solar radiation models. Sol Energy, 2004, 76: 423–453
26 Li C, Wang Z, Xu R, et al. The scientific information model of Chang'e-4 visible and near-IR imaging spectrometer (VNIS) and in-flight verification. Sensors, 2019, 19: 2806
27 Savitzky A, Golay M J E. Smoothing and differentiation of data by simplified least squares procedures. Anal Chem, 1964, 36: 1627–1639
28 Hapke B. Space weathering from Mercury to the asteroid belt. J Geophys Res, 2001, 106: 10039–10073
29 Pieters C M, Taylor L A, Noble S K, et al. Space weathering on airless bodies: resolving a mystery with lunar samples. Meteoritics Planet Sci, 2000, 35: 1101–1107

30 Clark R N, Roush T L. Reflectance spectroscopy: quantitative analysis techniques for remotesensing applications. J Geophys Res, 1984, 89: 6329–6340
31 Clark R N, Swayze G A, Livo K E, et al. Imaging spectroscopy: earth and planetary remote sensing with the USGS Tetracorder and expert systems. J Geophys Res, 2003, 108: 5131
32 McCord T B, Clark R N, Hawke B R, et al. Moon: near-infrared spectral reflectance, a first good look. J Geophys Res, 1981, 86: 10883–10892
33 Sunshine J M, Pieters C M, Pratt S F. Deconvolution of mineral absorption bands: an improved approach. J Geophys Res, 1990, 95: 6955–6966
34 Kaur P, Bhattacharya S, Chauhan P, et al. Mineralogy of Mare Serenitatis on the near side of the Moon based on Chandrayaan-1 Moon Mineralogy Mapper (M^3) observations. Icarus, 2013, 222: 137–148
35 Wu Y, Li L, Luo X, et al. Geology, tectonism and composition of the northwest Imbrium region. Icarus, 2018, 303: 67–90
36 Zhang X Y, Ouyang Z Y, Zhang X M, et al. Study of the continuum removal method for the Moon Mineralogy Mapper (M^3) and its application to Mare Humorum and Mare Nubium. Res Astron Astrophys, 2016, 16: 115
37 Besse S, Sunshine J M, Staid M I, et al. Compositional variability of the Marius Hills volcanic complex from the Moon Mineralogy Mapper (M^3). J Geophys Res, 2011, 116: 13
38 Cheek L C, Donaldson Hanna K L, Pieters C M, et al. The distribution and purity of anorthosite across the Orientale basin: new perspectives from Moon Mineralogy Mapper data. J Geophys Res Planets, 2013, 118: 1805–1820
39 Horgan B H N, Cloutis E A, Mann P, et al. Near-infrared spectra of ferrous mineral mixtures and methods for their identification in planetary surface spectra. Icarus, 2014, 234: 132–154
40 Pelkey S M, Mustard J F, Murchie S, et al. CRISM multispectral summary products: parameterizing mineral diversity on Mars from reflectance. J Geophys Res, 2007, 112: 14
41 Salvatore M R, Mustard J F, Wyatt M B, et al. Definitive evidence of Hesperian basalt in Acidalia and Chryse planitiae. J Geophys Res, 2010, 115: E07005
42 Cloutis E A, Gaffey M J. Pyroxene spectroscopy revisited-spectral-compositional correlations and relationship to geothermometry. J Geophys Res, 1991, 96: 22809–22826
43 Gaffey M J, Bell J F, Brown R H, et al. Mineralogical variations within the S-type asteroid class. Icarus, 1993, 106: 573–602
44 Varatharajan I, Srivastava N, Murty S V S. Mineralogy of young lunar mare basalts: assessment of temporal and spatial heterogeneity using M^3 data from Chandrayaan-1. Icarus, 2014, 236: 56–71
45 Pieters C M, Englert P A J. Remote Geochemical Analysis, Elemental and Mineralogical Composition. Cambridge: Cambridge University Press, 1993
46 Adams J B, Goullaud L H. Plagioclase feldspars-visible and near infrared diffuse reflectance spectra as applied to remote sensing. In: Proceedings of the 9th Lunar and Planetary Science Conference, 1978. 2901–2909
47 Donaldson Hanna K L, Cheek L C, Pieters C M, et al. Global assessment of pure crystalline plagioclase across the Moon and implications for the evolution of the primary crust. J Geophys Res Planets, 2014, 119: 1516–1545
48 Ohtake M, Matsunaga T, Haruyama J, et al. The global distribution of pure anorthosite on the Moon. Nature, 2009, 461: 236–240
49 Tompkins S, Pieters C M. Spectral characteristics of lunar impact melts and inferred mineralogy. Meteoritics Planet Sci, 2010, 45: 1152–1169
50 Adams J B, Horz F, Gibbons R V. Effects of shock-loading on the reflectance spectra of plagioclase, pyroxene, and glass. In: Proceedings of the 10th Lunar and Planetary Science Conference, 1979. 1–3
51 Johnson J R, Hörz F. Visible/near-infrared spectra of experimentally shocked plagioclase feldspars. J Geophys Res, 2003, 108: 5120
52 Crown D A, Pieters C M. Spectral properties of plagioclase and pyroxene mixtures and the interpretation of lunar soil spectra. Icarus, 1987, 72: 492–506
53 Klima R L, Pieters C M, Dyar M D. Spectroscopy of synthetic Mg-Fe pyroxenes I: spin-allowed and spin-forbidden crystal field bands in the visible and near-infrared. Meteoritics Planet Sci, 2007, 42: 235–253
54 Klima R L, Pieters C M, Dyar M D. Characterization of the 1.2 μm M1 pyroxene band: extracting cooling history from near-IR spectra of pyroxenes and pyroxene-dominated rocks. Meteoritics Planet Sci, 2008, 43: 1591–1604
55 Gross J, Treiman A H, Mercer C N. Lunar feldspathic meteorites: constraints on the geology of the lunar highlands, and the origin of the lunar crust. Earth Planet Sci Lett, 2014, 388: 318–328
56 Shearer C K, Elardo S M, Petro N E, et al. Origin of the lunar highlands Mg-suite: an integrated petrology, geochemistry, chronology, and remote sensing perspective. Am Miner, 2015, 100: 294–325
57 Shearer C K, Hess P C, Wieczorek M A, et al. Thermal and magmatic evolution of the Moon. Rev Mineral GeoChem, 2006, 60: 365–518
58 Lemelin M, Lucey P G, Gaddis L R, et al. Global map products from the Kaguya multiband imager at 512 ppd: Minerals, FeO, and OMAT. In: Proceedings of the 47th Lunar and Planetary Science Conference, 2016. 2994
59 Lucey P G. Mineral maps of the Moon. Geophys Res Lett, 2004, 31: L08701
60 Bickel C E, Warner J L, Phinney W C. Petrology of 79215-Brecciation of a lunar cumulate. In: Proceedings of Lunar and Planetary Science Conference, 1976. 7: 1793–1819
61 Dymek R F, Albee A L, Chodos A A. Comparative petrology of lunar cumulate rocks of possible primary origin-Dunite 72415, troctolite 76535, norite 78235, and anorthosite 62237. In: Proceedings of Lunar and Planetary Science Conference, 1975. 6: 301–341

62 Takeda H, Miyamoto M. Inverted pigeonites from lunar breccia 76255 and pyroxene-crystallization trends in lunar and achondritic crusts. In: Proceedings of Lunar and Planetary Science Conference, 1977. 8: 2617–2626
63 Warner J L, Simonds C H, Phinney W C. Apollo 17, Station 6 boulder sample 76255-Absolute petrology of breccia matrix and igneous clasts. In: Proceedings of Lunar and Planetary Science Conference, 1976. 7: 2233–2250
64 Nakamura Y, Kushiro I. Equilibrium relations of hypersthene, pigeonite and augite in crystallizing magmas: microprobe study of a pigeonite andesite from Weiselberg, Germany. American Mineralogist, 1970, 55: 1999–2015
65 Hawke B R, Blewett D T, Lucey P G, et al. The origin of lunar crater rays. Icarus, 2004, 170: 1–16
66 Wilhelms D E, John F, Trask N J. The Geologic History of the Moon. United States Geological Survey, 1987
67 Morrison D A. Did a thick South Pole-Aitken basin melt sheet differentiate to form cumulates? In: Proceedings of the 29th Lunar and Planetary Science Conference, 1998. 1657
68 Vaughan W M, Head J W, Wilson L, et al. Geology and petrology of enormous volumes of impact melt on the Moon: a case study of the Orientale basin impact melt sea. Icarus, 2013, 223: 749–765
69 Vaughan W M, Head J W. Impact melt differentiation in the South Pole-Aitken basin: Some observations and speculations. Planet Space Sci, 2014, 91: 101–106